

JGR Earth Surface

RESEARCH ARTICLE

10.1029/2020JF005675

Key Points:

- Mesoscale atmospheric processes such as narrow cold frontal rainbands play key roles in triggering landscape responses
- One such event in the Tuolumne River canyon, California, generated >500 landslides and 1.5–16 times the usual annual sediment yield
- Predictions of extreme, hazardous landscape response will benefit by incorporating mesoscale atmospheric processes driving intense rainfall

Supporting Information:

- Supporting Information S1
- Data Set S1
- Data Set S2
- Data Set S3

Correspondence to:

B. D. Collins,
bcollins@usgs.gov

Citation:

Collins, B. D., Oakley, N. S., Perkins, J. P., East, A. E., Corbett, S. C., & Hatchett, B. J. (2020). Linking mesoscale meteorology with extreme landscape response: Effects of Narrow Cold Frontal Rainbands (NCFR). *Journal of Geophysical Research: Earth Surface*, 125, e2020JF005675. <https://doi.org/10.1029/2020JF005675>

Received 1 MAY 2020

Accepted 17 SEP 2020

Accepted article online 4 OCT 2020

Linking Mesoscale Meteorology With Extreme Landscape Response: Effects of Narrow Cold Frontal Rainbands (NCFR)

Brian D. Collins¹ , Nina S. Oakley² , Jonathan P. Perkins¹ , Amy E. East³ , Skye C. Corbett¹ , and Benjamin J. Hatchett⁴ 

¹Geology, Energy, Minerals, and Geophysics Science Center, U.S. Geological Survey, Moffett Field, CA, USA, ²Scripps Institution of Oceanography, Center for Western Weather and Water Extremes, University of California, San Diego, La Jolla, CA, USA, ³Pacific Coastal and Marine Science Center, U.S. Geological Survey, Santa Cruz, CA, USA, ⁴Western Regional Climate Center, Desert Research Institute, Reno, NV, USA

Abstract Landscapes evolve in response to prolonged and/or intense precipitation resulting from atmospheric processes at various spatial and temporal scales. Whereas synoptic (large-scale) features (e.g., atmospheric rivers and hurricanes) govern regional-scale hydrologic hazards such as widespread flooding, mesoscale features such as thunderstorms or squall lines are more likely to trigger localized geomorphic hazards such as landslides. Thus, to better understand relations between hydrometeorological drivers and landscape response, a knowledge of mesoscale meteorology and its impacts is needed. Here we investigate the extreme geomorphic response associated with one type of mesoscale meteorological feature, the narrow cold frontal rainband (NCFR). Resulting from low-level convergence and shallow convection along a cold front, NCFRs are narrow bands of high-intensity rainfall that occur in midlatitude areas of the world. Our study examines an NCFR impacting the Sierra Nevada foothills (California, USA) that initiated over 500 landslides, mobilized ~360,000 metric tons of sediment to the fluvial system (as much as 16 times the local annual sediment yield), and severely damaged local infrastructure and regional water transport facilities. Coupling geomorphological field investigations with meteorological analyses, we demonstrate that precipitation associated with the NCFR was both intense (maximum 15 min intensity of 70 mm/hr) and localized, resulting in a highly concentrated band of shallow landsliding. This meteorological phenomenon likely plays an important role in landscape evolution and hazard initiation. Other types of mesoscale meteorological features also occur globally and offer new avenues for understanding the effects of storms on landscapes.

Plain Language Summary Major storms can cause extreme and hazardous landscape disturbances, but links between storm conditions and landscape response such as erosion and landslides remain poorly constrained. This is partly due to the lack of attention generally given to the finer-scale details of storms. We examined one type of atmospheric feature that is common in western North America (as well as in other regions), the narrow cold frontal rainband, and studied its effects on the landscape. In 2018, one such event in the Tuolumne River watershed, California, caused more than 500 landslides in a narrow area, moving more sediment in one day than the river would normally transport in a year. We find that landscape change, including potentially hazardous events such as landslides, can be driven primarily by fine-scale rainfall patterns rather than by the larger-scale storm conditions. More integration between weather and landscape scientists can advance knowledge of how storms influence landscapes and produce hazards, especially during extreme events.

1. Introduction

Landscape response from hydrometeorological disturbances can be extreme but is notoriously difficult to predict (e.g., Hooke, 2015; Lisenby et al., 2018; Phillips, 2006; Schumm, 1979; Wohl, 2013). Understanding and predicting nonlinear landscape response to forcing events such as severe storms is a long-standing problem in geomorphology, which has important implications for hazard assessment. Our ability to predict the geomorphic effects of severe storms depends on identifying and forecasting the meteorological conditions that cause them. Whether from landslide initiation, subsequent debris flow mobilization, or eventual

©2020 The Authors.

This is an open access article under the terms of the Creative Commons Attribution License, which permits use, distribution and reproduction in any medium, provided the original work is properly cited.

sediment input into fluvial systems, the geomorphic changes associated with extreme precipitation can lead to significant hazards to people and infrastructure and can have lasting effects on landscapes. Historically, geomorphologists and hazard planners have focused their efforts on identifying the presence of intense precipitation without in-depth consideration of its meteorological origins. For example, although many studies have defined rainfall thresholds for shallow landslides around the world (e.g., Guzzetti et al., 2008; Postance et al., 2018), they generally do not discuss through what meteorological processes these thresholds become exceeded. This is partially because detailed meteorological forcing mechanisms have yet to be directly associated with major landsliding events.

Improved forecasting and early warning of precipitation-related geomorphic hazards requires examination of the specific meteorological processes that lead to extreme rainfall. This can be achieved by linking the meteorological conditions to the land surface impacts through cross-disciplinary work. Moody et al. (2013) suggested that collaborative research between meteorologists and landslide scientists is necessary to advance the science connecting rainfall to mass movements, and some studies have begun to explore these connections. For example, Cordeira et al. (2019) showed that 82% of the days in which landslides occurred over a 142-year period in the San Francisco Bay area of California were associated with landfalling atmospheric river (AR) storms (e.g., Ralph & Neiman, 2005; Zhu & Newell, 1998). As conduits of significant water vapor to the west coast of the United States, ARs—thousands of kilometers long and hundreds of kilometers wide—are synoptic-scale features now recognized as diagnostic for hazard prediction given their relation to high storm total precipitation (e.g., Ralph et al., 2013). However, landslides and other landscape responses do not depend solely on storm total precipitation, and notably, many ARs do not cause landslides (e.g., Oakley, Lancaster, et al., 2018). Rather, rainfall rates (i.e., rainfall intensity) within a storm are well known to be the determining factor in predicting flash floods and debris flow initiation (e.g., Caine, 1980; Cannon, 1988; Guzzetti et al., 2008; Norbiato et al., 2008). Identifying the storm characteristics that bring high-intensity precipitation to vulnerable areas is therefore essential to hazard prediction and mitigation. Such precipitation is typically driven by atmospheric features at a finer scale than that which encompasses ARs, referred to as the mesoscale. Features of interest at this scale are often a few to hundreds of kilometers in horizontal extent and last between an hour to a day in duration; examples of mesoscale features include fronts, thunderstorms, squall lines, and precipitation bands within tropical and extratropical cyclones (cyclones are rotating areas of low barometric pressure).

Here, we explore the geomorphic effects of one type of mesoscale atmospheric feature known as a narrow cold frontal rainband (NCFR) that occurs in association with midlatitude (extratropical) cyclones. Midlatitude cyclones are important contributors to the weather in many regions of the world (including most of the USA, Canada, Europe, Chile, Australia, and other areas) and produce a variety of precipitation structures including rainbands. NCFRs are one type of rainband (Hobbs, 1978; Houze et al., 1976) that, if present, can produce the highest rainfall intensities within an extratropical cyclone (e.g., Hobbs, 1978; Houze et al., 1976; James & Browning, 1979; Rutledge & Hobbs, 1984). NCFRs are thus of substantial importance for geomorphologic and landslide hazard studies focused on the effects of rainfall on landscape response. However, NCFRs have seen only minor attention from these scientific research communities, despite their devastating consequences. For example, the January 2018 debris flows that killed 23 persons in Montecito, California, USA, resulted from an NCFR on a postwildfire landscape (Kean et al., 2019; Oakley, Cannon, et al., 2018).

Using a case study of an NCFR from northern California, USA, that caused hundreds of landslides (Figure 1) and tens of millions of dollars in infrastructure damage, we discuss general characteristics of NCFRs and investigate their impacts to demonstrate an emerging link that exists between mesoscale meteorology and extreme landscape response. To characterize the impacts from this event and document the spatial and site-specific characteristics of landslides caused by the NCFR, we mapped the induced landslide distribution using satellite imagery and conducted field investigations (measuring landslide geometry and soil infiltration parameters, and conducting soil characterization on field samples). We then analyzed the synoptic and mesoscale characteristics of the storm to identify those most important for the observed landscape response. Our study is motivated by the needs of the hazard planning community to interface with the atmospheric, hydrologic, and geomorphologic fields for improved hazard prediction and to better understand the implications of heterogeneously distributed rainfall on landscape evolution models. Further, we make the case that NCFRs and other mesoscale features demand more attention by

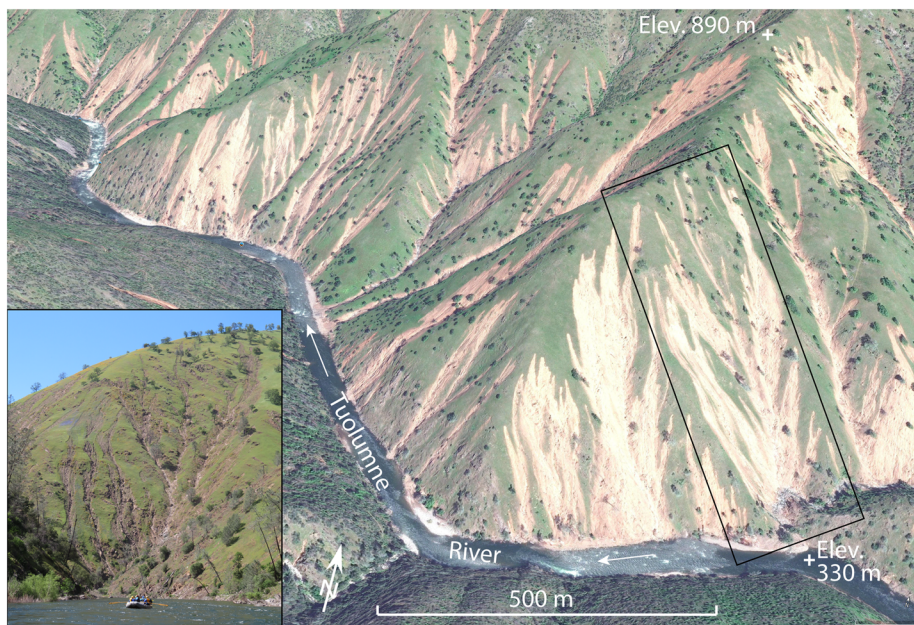


Figure 1. Oblique image of the hundreds of shallow landslides within the Tuolumne River canyon north of Groveland, California, caused by the 22 March 2018 NCFR. Inset image shows view taken from river level on 21 April 2019 of the area encompassed by the black rectangle. Oblique image from GeoEye taken on 17 April 2018.

those studying landscape response, not only in the western U.S. study area on which we focus but also globally.

2. Meteorological Concepts and NCFR

To understand the drivers of short-duration, high-intensity precipitation processes described herein and that are of particular interest to geomorphology and landslide hazards, we look to mesoscale meteorology. The mesoscale encompasses a horizontal scale from 2 to 200 km and a temporal scale of ~1 hr to 1 day (Thunis & Bornstein, 1996). Although other definitions exist for the mesoscale (e.g., Lin, 2007, and references therein), we adopt a definition that is both contemporary and relevant to the study at hand. Atmospheric features and processes often span and interact over multiple scales, but in general, the mesoscale distinguishes itself from the synoptic scale in that motions are driven by many different mechanisms rather than by just one dominant process (Markowski & Richardson, 2010).

NCFRs are one type of mesoscale phenomenon that occur along cold fronts of synoptic-scale midlatitude cyclones. As a defining characteristic for midlatitude cyclones, cold fronts (the boundary formed between colder air and the warmer air that it replaces) commonly bring precipitation in particular locations relative to the front. An NCFR, if present, will be found coincident with and parallel to the cold front of the cyclone (Hobbs, 1978). In radar imagery, NCFRs can be recognized as narrow ribbons of high reflectivity (>40–50 dBZ, coinciding with moderate to heavy rain rates; Figure 2). They are generally 3–5 km wide and may extend up to 100–200 km in length, but are typically on the order of several tens of kilometers long and broken up into characteristic “gaps and cores” (e.g., Browning, 1986; Hobbs & Biswas, 1979; Jorgensen et al., 2003; Locatelli et al., 1995). The “cores” are areas of high reflectivity and intense rainfall, whereas “gaps” feature lighter rainfall. Precipitation cores can be a few kilometers to more than 100 km long (James & Browning, 1979) and are relatively parallel, though generally offset from one another, creating a zigzag or scalloped appearance. The gaps between cores may extend from less than 20 km to more than 50 km (Locatelli et al., 1995). NCFRs are characterized by relatively shallow (generally <3 km vertically) yet vigorous convection, producing high-intensity precipitation (Browning & Harrold, 1970; Marécal et al., 1993). During an NCFR in Washington, USA, Hobbs and Persson (1982) recorded 2-min precipitation rates of 45 mm/hr⁻¹, and an event in Virginia and Maryland, USA, had recorded 5- to 10-min rates of 100 mm hr⁻¹ (Koch & Kocin, 1991). NCFR occurrence is widespread in midlatitudes, and these features

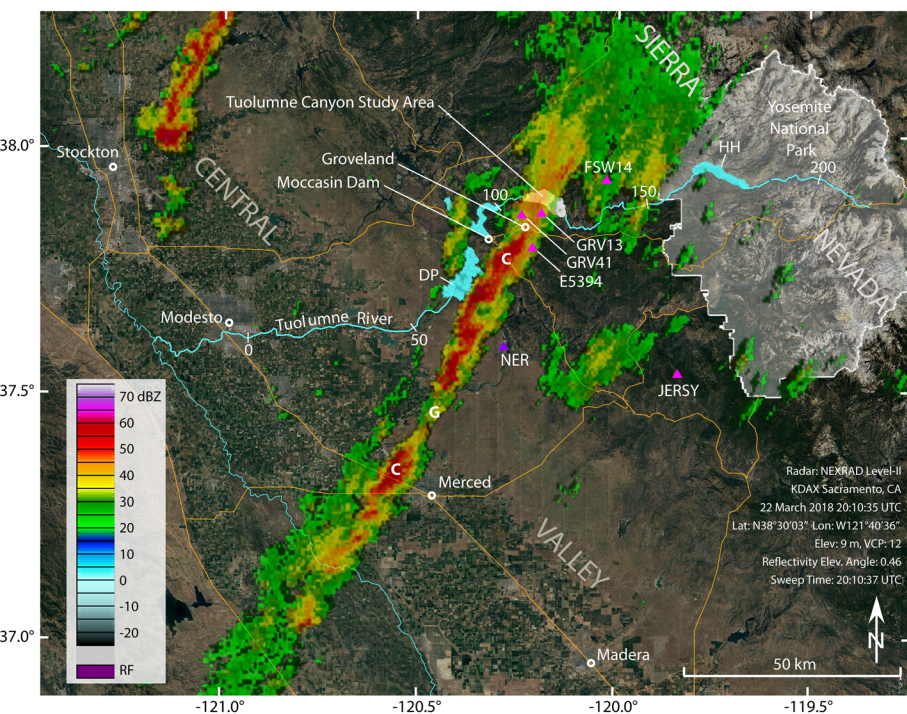


Figure 2. Regional mesoscale map of the 22 March 2018 NCFR in the vicinity of Groveland, California, at 20:10 UTC (1:10 p.m. local time—PDT). Cores (C) and gaps (G) are visible in the NCFR and the structure aligns with the impacted study area featuring the concentrated landslide distribution (Figure 1). Radar data are shown in dBZ reflectivity units (here, 40 dBZ \approx 12 mm/hr and 50 dBZ \approx 37 mm/hr, indicative of very intense rainfall; RF indicates “radio frequency,” equivalent to noise). Pink triangles indicate locations of rain gauges as listed in Figure 5. The purple triangle is the location of New Exchequer Dam (NER) used for supplemental meteorological observations. Numbers along Tuolumne River coincide with distances in km along the long profile shown in Figure 8. DP = Don Pedro Reservoir, HH = Hetch Hetchy Reservoir. Radar data are from NOAA (<https://www.cnrfc.noaa.gov/radarArchive.php>; accessed on 18 March 2020).

have been well observed in field campaigns in the western United States (Hobbs & Persson, 1982) and elsewhere—e.g., the United Kingdom (James & Browning, 1979), France (Roux et al., 1993), Germany (Gatzen, 2011), and Chile (Viale et al., 2013). Though no climatology exists for NCFR activity along the west coast of the United States, anecdotal reports from the operational weather forecast community suggest several events occur each year. Despite the recognition that NCFRs are important meteorological events, little work has been done relating them to geomorphic hazards.

3. Event Setting

The NCFR storm event examined in detail herein occurred on 22 March 2018 and impacted the Sierra Nevada foothills in central California, near the town of Groveland (Figure 2). The Groveland area (elevation 870 m) is characterized by steep, rugged terrain and is located at the top of a step in relief (gaining \sim 600 m in 7 km) where the Sierra Nevada begins to rise to the east, away from the relatively flat Central Valley to the west (Figure 2). The Tuolumne River cuts through a 700-m-deep canyon located 6 km north of Groveland, and drains a large part of Yosemite National Park, situated to the east. Flows in the river are regulated upstream by several dams (including one that forms Hetch Hetchy Reservoir—the drinking water source for the city of San Francisco located 230 km to the west) and downstream by Don Pedro Reservoir, an irrigation source for agriculture in the Central Valley.

The 22 March 2018 NCFR affected terrain in and around Groveland and along the slopes of the Tuolumne River canyon. The canyon slopes are covered by conifer forest and dense chaparral woodlands on the south side, and grasses with sparse chaparral vegetation on the north side. The area was affected by wildfire in 2013; however, local burn severity was low on the hillslopes that underwent landsliding in

2018 (Abney et al., 2019; Staley, 2013). Hillslopes are underlain by mostly metamorphic assemblages of the Paleozoic Shoo Fly and Calaveras Complexes (Wagner et al., 1991). Exposed rock types consist of slates and phyllites, and soils are generally either weathered in place or colluvial, consisting of gravelly low-plasticity clays and silty sands (additional details available in the supporting information, Text SA). The metasedimentary rocks in the canyon contain gold-bearing veins originating in the basement plutonic rocks of the region. These veins were the source of vast lode and subsequent placer gold deposits that made California famous during the mid-1800s gold rush (U.S. Geological Survey, 1897). The river corridor therefore has historical significance, with remnants of mining infrastructure and trails located throughout the bottom of the canyon. Due to the river's scenic, geologic, recreational, and cultural resources, the Tuolumne River was designated a Wild and Scenic River in 1984. Today, the river hosts a commercial river-running industry and serves as a conduit for drinking and irrigation water projects. As such, the sediment load of the river is a concern for water resource managers (NPS, 2013; Wright & Marineau, 2019).

4. Storm Characterization

4.1. Synoptic Setting

A midlatitude cyclone featuring a strong AR moved across the northeast Pacific Ocean and made landfall in central California at approximately 18:00 UTC on 20 March 2018. The AR had integrated water vapor transport (IVT; Zhu & Newell, 1998) greater than 700 kg/m/s (where IVT values of 500–750 kg/m/s indicate a strong AR; Ralph et al., 2019) and remained nearly stationary over the Central Coast for ~48 hr (Figure 3a). This portion of the storm event produced copious rainfall across much of the state, including over 100 mm in the study area. Precipitation during this time was predominantly associated with orographic lifting of moist air by the Sierra Nevada (e.g., Neiman et al., 2013; Ralph et al., 2006) and synoptic-scale ascent. By 12:00 UTC 22 March 2018, the AR began to move to the southeast and by the time the NCFR formed around 18:00 UTC, the core of the AR was situated over southern California (Figure 3b). However, a secondary but much weaker moisture plume had developed north of the main AR and overhead of the study area by 18:00 UTC (Figure 4) and the overall synoptic conditions (e.g., divergent upper level air flow) were favorable for intense precipitation in the Groveland-Sierra Nevada foothills region (see supporting information Text SB, Figures SB1 and SB2).

4.2. Mesoscale Setting

The NCFR feature that produced the high-intensity rainfall in the Groveland area beginning at 18:00 UTC on 22 March 2018 was associated with the passage of a cold front. In situ meteorological observations are sparse in the area of the landslide observations, so we relied primarily on observations from stations located elsewhere in the Central Valley in conjunction with atmospheric reanalysis products to document the frontal passage (see supporting information Text SB, Figures SB3 and SB4). A surface-based weather station with observations at high temporal resolution, located 35 km to the southwest of the study area at New Exchequer Dam (Figure 2, site NER; NOAA, 2020), indicates the passage of a cold front between 21:00 and 22:00 UTC 22 March 2018 (about 1 hr after impacting the study area). This is demonstrated by an abrupt shift in wind direction from southeast (~120°) to northwest (~300°), accompanied by a rapid temperature drop and burst of precipitation (see Text SB, Figure B3). The surface cold front along which this NCFR occurred was likely modified and retarded due to its interaction with the complex terrain of California, including the Sierra Nevada (e.g., Neiman et al., 2004; Schumacher et al., 1996). NCFRs are driven by convergence of low-level flow along the cold front resulting in upward vertical motions and shallow but intense convection (Jorgensen et al., 2003; Locatelli et al., 1995; Persson et al., 2005). Evidence for low-level convergence during the 22 March 2018 NCFR is presented in Text SB (Figures SB5 and SB6). Convergence and convection along the front were the primary processes driving the intense rainfall. This assertion is supported by the orientation of the NCFR normal to the Sierra Nevada (Figure 2) and extending southwestward over the low terrain of the Central Valley. In a primarily orographically driven scenario, we would expect intense precipitation to be oriented parallel to the mountain barrier. While orographic forcing does not appear to be the dominant process, we cannot rule out that both convergence along the front and orographic processes were simultaneously active in producing intense precipitation in the study area.

Radar reflectivity imagery indicate that the NCFR formed in the Central Valley by 17:30 UTC and moved from northwest to southeast along the Sierra Nevada front. The feature itself had a southwest to northeast

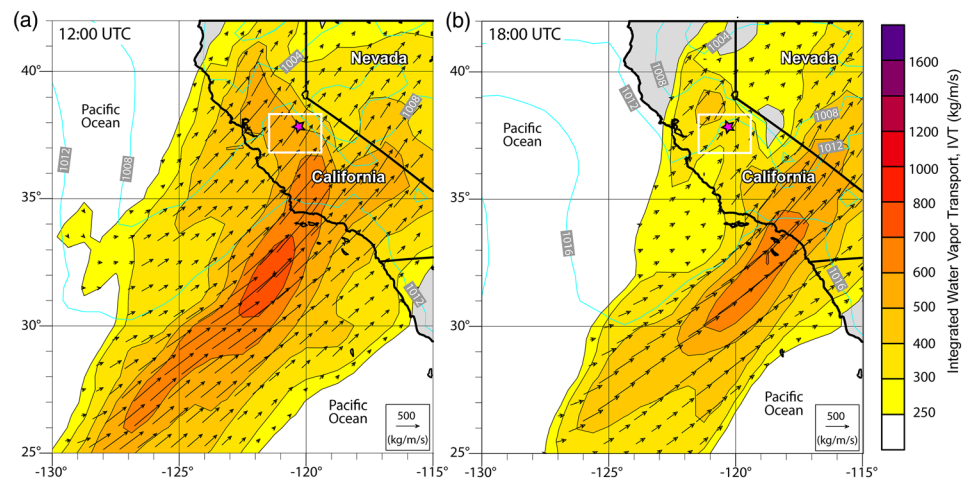


Figure 3. Meteorological synoptic maps of the East Pacific Ocean and California region showing sea level pressure (hPa; blue contours) and integrated water vapor transport (IVT; kg/m/s; vectors and filled contours) at two time slices. The data in (a) depict a broad atmospheric river (AR) impacting California at 12:00 UTC 22 March 2018, roughly 6 hr prior to NCFR formation. In (b) the AR has moved to the south around the time of NCFR formation (18:00 UTC). White boxes over California indicate the extent of the study area displayed in Figure 2. Purple stars represent the location of the town of Groveland. Atmospheric reanalysis from the NASA Modern-Era Retrospective analysis for Research and Applications version 2 (MERRA-2; Gelaro et al., 2017).

orientation as it approached the study area (Figure 2). By 18:00 UTC, the NCFR was over the area of interest (Groveland and the area immediately north) and persisted there until ~21:00 UTC, when it continued southeast along the Sierra front. During that time, radar reflectivity exceeded 50 dBZ (see radar time slices

in Figure 5), indicative of heavy rainfall and possible hail. The characteristic sinuous shape of the NCFR and the presence of gaps and cores are apparent intermittently in radar reflectivity during this time (Figure 2). However, the NCFR stalled over the study area by ~18:30 UTC, becoming a nearly continuous line of intense rainfall more than 100 km long. As the NCFR and front stalled, we infer a shift from shallow to deeper convection, as indicated by decreasing cloud top temperatures in satellite imagery (see Text SB, Figure SB7).

4.3. Precipitation Observations

Passage of the AR and the NCFR were recorded at several rain gauges near the study area (Table 1; Figure 5) and via radar (Text SB, Figures SB8 and SB9). Storm precipitation began on 21 March 2018 and by 00:00 UTC on 22 March 2018, up to 25 mm accumulation had occurred. AR-related rainfall was mostly moderate (15-min intensities <10 mm/hr, Figure 5) for the next 18 hr until the NCFR impacted the Sierra Nevada foothills around 18:00 UTC 22 March 2018. Despite the moderate rainfall intensities during the lead-up to NCFR arrival, the antecedent storm totals were substantial: between 70 and 140 mm of rainfall were recorded between 00:00 UTC on 21 March 2018 and 18:00 UTC on 22 March 2018 in the region (Figure 5). The precipitation duration and total likely saturated a substantial portion of the shallow soils (which average only ~0.4 m thick; Text SC) in the Tuolumne River canyon. Thus, when the more intense rainfall associated with the NCFR passage arrived after 18:00 UTC, it fell on already highly susceptible soils with regard to positive pore water pressure generation. This likely facilitated both slope failure and overland flow.

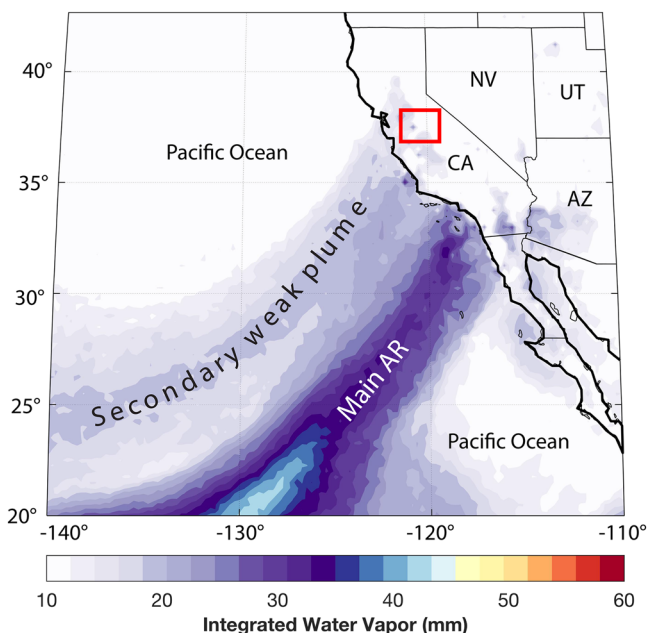


Figure 4. Satellite-derived integrated water vapor (IWV) at 20:00 UTC 22 March 2018 from the MIMIC-TPW2 product (University of Wisconsin, 2020; Wimmers & Velden, 2011). IWV indicates the total depth of water that could be condensed out of a vertical column of the atmosphere and is related to the expected precipitation from a storm. Red box indicates general area of interest to this study and approximate to the bounds of Figure 2. Note that satellite-derived water vapor is not well-resolved over land, giving the appearance of the moisture plumes weakening or disappearing over land.

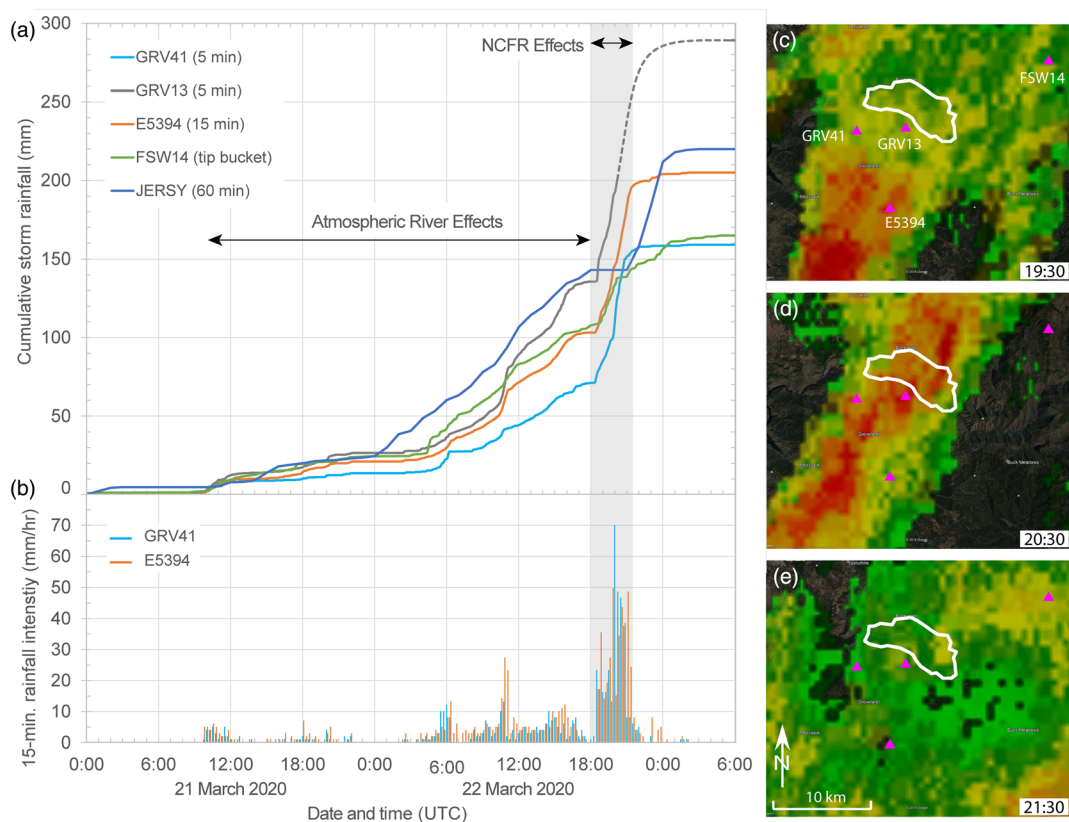


Figure 5. (a) Cumulative rainfall records for the 22 March 2018 NCFR storm at five rain gauges and (b) rainfall intensity at two gauges located near the observed landslide distribution in the Tuolumne River canyon (white outline in radar images—see also Figure 2). Only the storm total (289 mm) was recorded after 20:11 UTC for GRV13 and we extrapolate a plausible record (dashed curve). Time resolution of each rain gauge is provided in parentheses. (c–e) Radar time series images during the passage of the NCFR. Radar data color scheme and parameters are as for Figure 2. All times are in UTC.

Rainfall intensities during the NCFR in the Groveland area were both high and transient. The maximum 15-min precipitation recorded in the region was 70 mm/hr at GRV41 occurring at 20:00 UTC 22 March 2018. Maximum 1-hr observations at the E5394 and JERSY stations (located 5 and 48 km southeast of Groveland, respectively; Figure 2) reached 41 and 28 mm, respectively, as the NCFR moved through the region between 20:00 UTC 22 March 2018 (E5394) and 00:00 UTC 23 March 2018 (JERSY). During 45-min periods between ~20:00 to 21:00 UTC, 15-min intensities averaged 44 and 51 mm/hr at stations E5394 and GRV41, respectively (Figure 5). The station closest to the landslides in the Tuolumne River canyon (GRV13) stopped reporting data for a 10-hr period beginning at 20:11 UTC and missed the core of

Table 1
Summary of Precipitation Gauges Analyzed in Figure 5

Gauge ID and abbreviation	Elevation (m)	Observation interval	Distance from landslides (km)	Network and source
KCAGROVE41 (GRV41)	850	5 min	7	Weather Underground (WU) https://www.wunderground.com/
KCAGROVE13 (GRV13)	880	5 min	3	Weather Underground (WU) https://www.wunderground.com/
EW5394 (E5394)	1,044	15 min	11	Citizen Weather Observer Program (CWOP) https://mesowest.utah.edu/
FSW14	1,318	tipping bucket	13	U.S. Forest Service 2013 Rim Fire Monitoring Program
Jerseydale (JERSY)	1,189	60 min	48	Remote Automated Weather Station (RAWS) https://raws.dri.edu/

the event. However, the station came back online after the rainband passed and recorded the highest storm total (289 mm) of all the stations. Although this total is suspect due to the outage and that it is significantly higher than other observations in the vicinity (Figure 5a), the precipitation total is also plausible given that the gauge's location is the closest to the most impacted part of the study area. If the gauge observations are accepted as valid, they provide further support for localization of the impacts.

5. Storm Impacts

The National Weather Service anticipated intense rainfall and impacts associated with this event and recognized the potential for an NCFR to cause debris flows within a postwildfire burned area located ~45 km southeast of the study area (the Detwiler burn area; Meadows et al., 2019). Warnings were issued for intense thunderstorms and heavy precipitation in the region and government agencies conducted evacuations in areas expected to receive the largest streamflows. Damage from the storm was intense but appears to have been narrowly focused and generally coincident with the passage of the NCFR. In addition to localized flooding that impacted businesses and washed out roads in the Groveland area, the heavy precipitation also damaged parts of the city of San Francisco's water delivery system downstream from Hetch Hetchy Reservoir. This included abnormal seepage from Moccasin Dam, located 7 km west of Groveland (Figure 2), that resulted in a flash flood warning and evacuations downstream in case the dam failed. Direct economic losses to infrastructure, including damage to Moccasin Dam, were estimated at \$74 million (Union Democrat, 2018).

Among the areas most intensely impacted from the NCFR was the Tuolumne River canyon, where we identified a dense concentration of landslides along the canyon slopes. Using high-resolution satellite imagery (collected via GeoEye on 17 April 2018) in a three-dimensional GIS platform (Google Earth), we manually mapped more than 500 landslides, each with a discrete initiation point, along a 9-km length of the river canyon (Figures 1 and 6). Hiking- and rafting-based field studies conducted of the area (see Texts SA and SD) revealed that the landslides were mostly of the shallow (0.2–0.6 m), debris slide-debris flow type (Varnes, 1978) overlying weathered phyllite bedrock and located predominantly on south-facing grass-covered slopes on the north side of the river (Figure 6b). Debris flows entrained substantial sediment along their runout paths, in total disturbing ~1 km² of land surface area (Text SD). This represents 4% of available land surface in this area of the river (as measured from the river to the canyon rim along the length of affected canyon). Although two additional storms occurred in April 2018 (6–7 April and 16–17 April, prior to collection of the satellite imagery; see also Hatchett, 2018) that might also have triggered landslides or released sediment to the river system, comparison of the satellite imagery (Figure 1) to that from oblique aerial photos taken the day after the NCFR (Figure 6a) reveal little in the way of significant changes between these points in time (23 March 2018 and 17 April 2018). Further, both April storms had much lower rainfall intensity compared to the 22 March 2018 NCFR (compare maximum of 13 mm/hr 15-min intensity at gauge E5394 during the 6–7 April 2018 storm to nearly 50 mm/hr during the NCFR; Figure 5), precluding a likely trigger for landsliding from the April storms.

The resultant sediment mobilization from the NCFR-induced landsliding deposited new debris fans and significantly aggraded existing ones at the river's edge (Figures 6c and 6d), modifying the morphology of some rapids. Sediment budget calculations for the flux of landslide material transported downslope (based on landslide area mapping and field measurements of a 0.4 m mean mobilized sediment depth; Text SC) indicate that ~360,000 metric tons (t) of material were mobilized to the river as a result of the storm (350,000 t of hillslope material mobilized by landsliding, and another ~10,000 t by bank erosion opposite a newly enlarged debris fan; see Text SC). Compared to the average annual sediment load of the river (based on measurements of suspended-sediment transport in previous years, and by decadal-scale sediment infilling of Don Pedro Reservoir downstream; HDR Engineering, Inc, 2012; U.S. Geological Survey, 2019; Wright & Marineau, 2019), we estimate that the single-day 22 March 2018 storm mobilized 1.5–16 times more sediment than this part of the Tuolumne River generally carries annually and up to 39 times more sediment than in a dry year. These estimates are especially noteworthy given that the hillslope area contributing sediment from the 22 March 2018 landslides (0.97 km²; Text SD) represents only 0.04% of the watershed area from which fluvial sediment load in this river reach could be derived (2,560 km² between large upstream dams and Don Pedro reservoir located downstream). If averaged over the basin area of 2,560 km²,

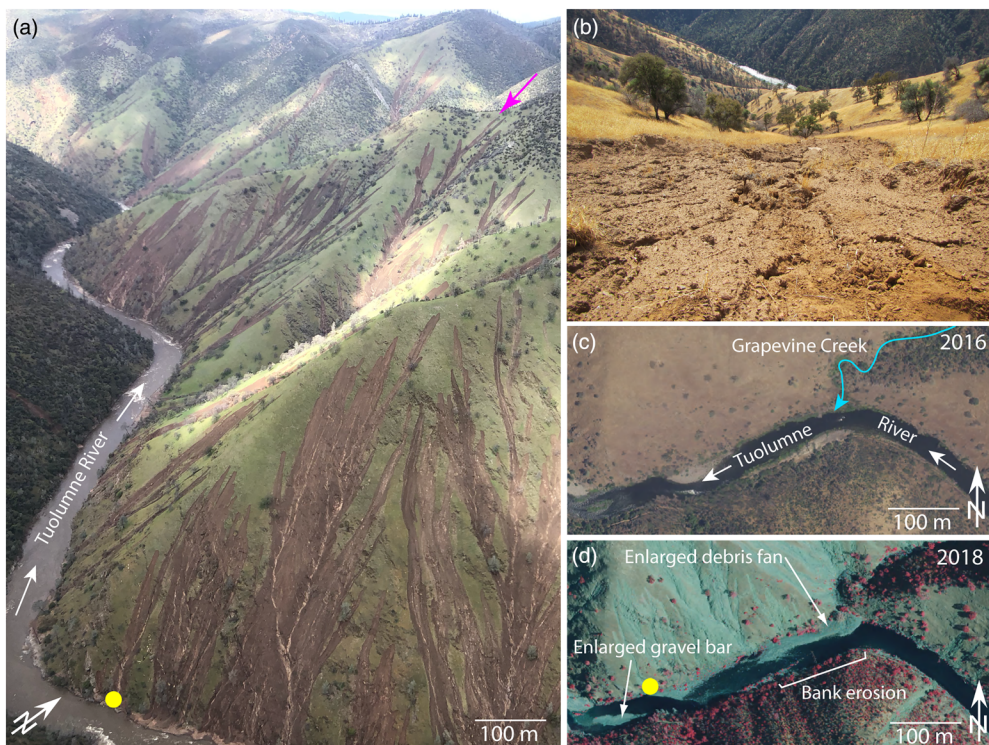


Figure 6. Examples of geomorphic effects from the 22 March 2018 storm in the Tuolumne River canyon. (a) Overview image taken one day after the storm showing shallow landslide and debris flow scars. Image credit: Wayne Handley (used with permission). (b) Detail of initiation zone for one landslide, where soil failed down to saprolite on a south facing hillslope covered with grass. Pink arrow in (a) identifies location and view angle of image. Panels (c) and (d) show aerial images of the confluence of the Grapevine Creek tributary with the Tuolumne River in 2016 (prestorm) and 2018 (poststorm), respectively (yellow dot identifies identical location in [a], see also bottom right area of Figure 1). In (d), compared to (c), landslides and debris flow channels are visible on hillslopes on both sides of the river, and the debris fan at the mouth of Grapevine Creek had enlarged greatly, as had a gravel bar 200 m downstream. Bank erosion occurred as the flow shifted toward river-left (south) in response to enlargement of the Grapevine Creek debris fan.

mobilizing 350,000 t of hillslope material equates to a sediment yield of 137 t/km² or a bedrock denudation rate of 52 mm/kyr (assuming bedrock density of 2,650 kg/m³). These are reasonable long-term values expected for a mountainous region experiencing a Mediterranean climate (Mollieix et al., 2017). However, those values indicate a remarkable erosion event given that they were generated not from the entire basin over a full year but rather from only 0.04% of the basin in one storm. That such a large mobilization of sediment mass could originate from such a small proportion of the watershed area indicates the capability of a short-lived, mesoscale storm feature to alter sedimentary and geomorphic systems to a substantial degree. The fluvial geomorphic effects of this storm also affected riparian habitat, as debris fans and cobble bars formed and enlarged; moreover, bank erosion (6,100 m³) opposite one greatly enlarged debris fan (Figure 6d) caused large trees to fall into the river. In mountain rivers, such changes to river morphology and bed composition directly control habitat complexity and viability of certain ecosystem components such as the survival of periphyton, benthic invertebrates, and fish eggs within the substrate (e.g., Bellmore & Baxter, 2014; Greig et al., 2005; Hauer et al., 2011; Spina, 2000).

6. Discussion

6.1. Synoptic and Mesoscale Influences on Landslide Triggering

The well-recorded rainfall time series of the synoptic (AR) and mesoscale (NCFR) meteorological features during the March 2018 storm, combined with observations collected during our field investigations, allow us to explore the surface and subsurface hydrological conditions that led to localized landsliding in the

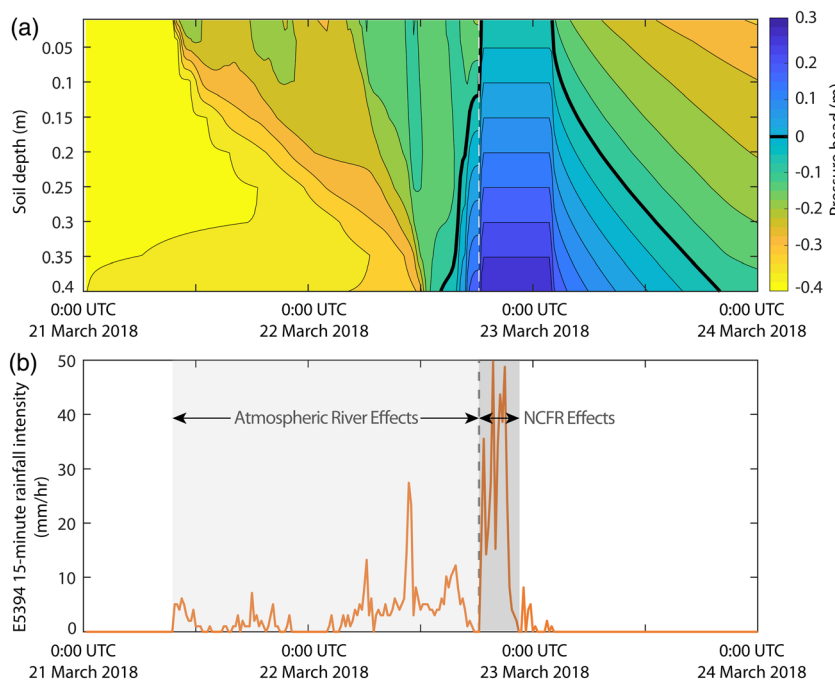


Figure 7. (a) Numerical model results showing the evolution of pressure head over time for a 1-D soil column subjected to the rainfall record shown in (b) (see E5394 station in Figures 2 and 5). The modeled soil column is 40 cm thick sandy loam with a saturated hydraulic conductivity of 20 mm/hr, overlying a 10 cm thick silt loam with a saturated hydraulic conductivity of 2 mm/hr, consistent with field measurements. Wetting of the soil through steady AR-related rainfall on 21 and 22 March 2018 fills the pore space of the soil column, increasing unsaturated hydraulic conductivity. This allows rapid transmission of water from the NCFR event beginning at ~18:00 UTC on 22 March 2018 (dashed line), which subsequently produces positive pore water pressure throughout the soil column and enables saturation excess overland flow. Thick black line indicates the evolution of the position of the water table (i.e., pore water pressure head equal to zero).

Tuolumne River canyon. For example, by comparing the storm's rainfall intensities to site-specific soil hydraulic conductivity values, we can evaluate the possible mechanisms that could have caused runoff (e.g., Mirus & Loague, 2013) and landslide initiation (e.g., Collins & Znidarčić, 2004). Measurements using a minidisk infiltrometer (see Text SA) revealed hydraulic conductivities of the soil surface in the range of 5 to 20 mm/hr—far lower than the rainfall intensities recorded during the peak of the NCFR. However, the 70–140 mm of antecedent rainfall that occurred during the 32 hr prior to the NCFR event occurred at much lower intensities (generally less than 10 mm/hr; Figure 5b) and may have led to near-complete saturation of the subsurface prior to NCFR arrival. Our measured value of hydraulic conductivity from the failure plane (2 mm/hr) suggests that ponding would have occurred in the absence of macroscale bedrock fractures. Thus, the higher rainfall intensities during the peak of the storm may have then caused pore water pressures to increase at the soil-bedrock interface, leading to landslide initiation. However, with measured rainfall intensities also greater than the saturated hydraulic conductivity of the soil surface, overland-flow-inducing erosion (e.g., Godt & Coe, 2007) also likely led to debris flow generation.

To examine how the progression of rainfall may have impacted soil pore water pressure evolution and runoff potential, we conducted a 1-D unsaturated zone hydrology simulation using the USGS program VS2Dt (e.g., Lappala et al., 1987). VS2Dt is a finite difference model that solves Richards equation for variably saturated subsurface water flow with time-varying boundary conditions. Our model domain consists of a 40 cm thick sandy loam ($K_s = 20$ mm/hr) overlying a 10 cm thick silt loam base ($K_s = 2$ mm/hr), with a gravity drainage boundary condition at the bottom of the domain. We utilized soil moisture constitutive relationships of van Genuchten-Mualem (van Genuchten, 1980) based on our measured soil textures (Text SA) and used the 15-min rainfall record from CWOP gauge E5394 (Table 1, Figures 5 and 7) to run

the model. The results show the progression of pore water pressure throughout the depth of the soil column (Figure 7). As the low-intensity rainfall begins on 21 March 2018 during the AR part of the event, the soil column gradually sees a reduction in suction (negative pressure head) as the infiltration front migrates downward and volumetric water content increases. This steady infiltration reaches the contact with the silt loam base (i.e., simulating a low-permeability bedrock interface), producing positive pore water pressure hours before the arrival of the NCFR part of the precipitation time series. Once the NCFR arrives, the model indicates that the soil column immediately becomes fully saturated with the perched water table reaching the ground surface, producing increased pore water pressure at the contact and enabling saturation-excess overland flow for the duration of the event. The model results therefore suggest that effective stress along the failure plane was fully reduced, increasing the likelihood of shallow landsliding. Additionally, the lack of available water storage in the soil may have shunted off the bulk of the NCFR rainfall as runoff, and infiltration excess overland flow caused by the high rainfall intensity accompanying the strongest pulses of the NCFR may also have occurred. This is consistent with our field observations for both discrete shallow landslide events as well as significant runoff-driven erosion and debris flows (Figure 6a). Therefore, the numerical simulation results show that the preceding AR event likely played an important role in preconditioning the soil for multiple failure modes upon the onset of the NCFR. However, although the strong AR was likely critical for reaching antecedent and potentially near-saturated soil conditions, it was not the driver of the intense precipitation that likely led to landsliding. Rather, landsliding and debris flow formation occurred under much weaker precipitable water vapor and moisture transport conditions during NCFR passage several hours after the AR had moved southward away from the study region (Figure 3b).

6.2. NCFR Influence on Landslide Distribution

Our evaluation of the 22 March 2018 Tuolumne River canyon event provides a diagnostic view of the direct impacts that a mesoscale meteorological feature such as an NCFR can have on geologic hazards and landscape response. Typically, regions of localized landsliding can be identified through analysis of susceptibility traits—for example, soil type and depth, rock type, vegetation, land use, regional relief, and topographic slope, convergence, and aspect (e.g., Guzzetti et al., 2005). Our field investigation revealed at least some commonalities that can be ruled out with respect to identifying why the landsliding occurred in such a narrow region. That is, some characteristics such as soil type and depth, and bedrock type, do not vary considerably throughout and in neighboring areas of the canyon. However, topographic aspect and vegetation apparently played a role in minimizing landslide initiation on the south (more densely vegetated) side of the canyon, where forest and chaparral likely intercepted precipitation before it was able to infiltrate the subsurface, and vegetation root strength (e.g., McGuire et al., 2016; Schmidt et al., 2001) would have resisted landslide-inducing shear stresses. Although wildfire had affected the area 5 years earlier (the 2013 Rim Fire), examination of burn severity and debris flow hazard maps (Abney et al., 2019; Staley, 2013) indicate low likelihood of increased susceptibility to landsliding in the vicinity of the documented landsliding. The dominant vegetation type (grasses) within the majority of the area affected by landsliding showed no changes following the fire (as indicated by historical satellite imagery), suggesting little chance of vegetation-type conversion processes that might have aided landslide initiation (e.g., Parise & Cannon, 2012). Further, other more heavily vegetated areas showed few signs of wildfire-related tree mortality that could have reduced slope stability (Casas et al., 2016; Shive et al., 2017). Thus, we conclude that postwildfire conditions did not likely instigate or exacerbate landsliding within the study region.

Canyon relief and hillslope gradient evidently did play roles in the localized landslide triggering. The landsliding appears to have coincided with both a small increase in canyon relief (Figure 8a) and a substantial increase in hillslope gradient (Figure 8b), with the area of landsliding from the storm nearly coincident with the maximum gradient of the canyon's side slopes. However, by overprinting the storm's rainfall characteristics along the same river canyon profile (Figure 8c), the contemporaneous mesoscale rainfall pattern also clearly aligns with the landslide distribution, thereby explaining its highly localized occurrence. Whereas the hillslope gradient is somewhat higher just upstream (near river profile at 122 km; Figure 8b), the rainfall intensity drops off substantially there compared to where the landslides occurred. Further, the area of landsliding is overprinted with multiple episodes of maximum rainfall compared to other areas—a result of the NCFR propagating southeastward along the Sierra Nevada range front and stalling over the study area.

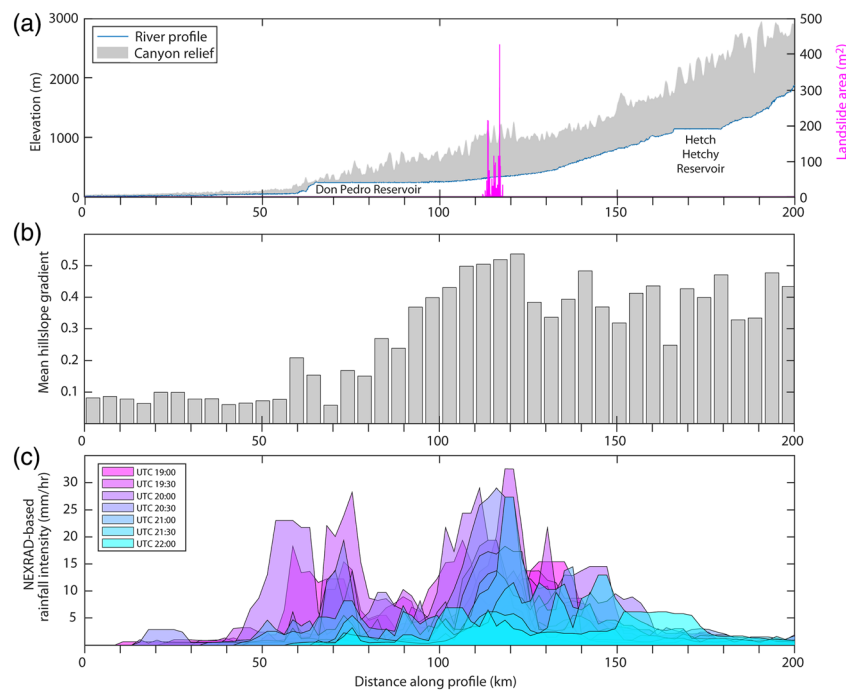


Figure 8. Conditions leading to severe landsliding from the 22 March 2018 NCFR. The longitudinal profile of the Tuolumne River is shown on the x axis beginning near the city of Modesto, 62 km downstream of Don Pedro Reservoir (Figure 2) and plotted versus (a) elevation and total area affected by landslides, (b) mean hillslope gradient of river canyon side slopes within 2.5 km of the channel thalweg, and (c) the 30-min increment time series of maximum instantaneous rainfall intensity within 2.5 km of the channel thalweg, calculated from NEXRAD radar reflectance using the “west coast cool stratiform” Z-R relationship (Matrosov et al., 2014). The landslide distribution (pink area in panel a) is shown in Figures 1 and 2 (white-shaded area). Topographic analysis performed with TopoToolbox (Schwanghart & Scherler, 2014). Additional explanation of methods is presented in the supporting information, Text SD.

Thus, the mesoscale attributes of the storm, via the development and stalling of the NCFR, support and can directly explain the extreme landslide response through massive localized landsliding and resultant sediment transport.

6.3. Broad-Scale NCFR Occurrence and Landscape Response

Based on observations and anecdotal reports from the operational meteorology community, NCFRs are relatively common in northern California (e.g., Blier, 2003; Blier et al., 2005; Jorgensen et al., 2003; King et al., 2009; White et al., 2003). Although a catalog of NCFR events has never been compiled (whether causing significant landscape response or not), we can point to another recent and nearby NCFR on 14 February 2019 (Hatchett et al., 2020) as evidence of their occurrence and consequence in the central Sierra region. The 14 February 2019 event also had radar reflectivity in excess of 50 dBZ in a narrow band (Figure 9), and traversed through the two counties (Calaveras and Amador) located northwest of Groveland, producing 10-min rainfall intensities approaching 60 mm/hr (MesoWest, 2019). As a result, some regional roads were closed for several days due to landslides and localized flooding, and the severity of damage led to state and federal disaster declarations. In 2004, another NCFR some 200 km to the west of Groveland near San Francisco also had extremely high rainfall intensities (5-min intensities of 128 mm/hr) and caused localized flash flooding and resultant damages exceeding \$27 million (Blier et al., 2005). Similar to the 22 March 2018 NCFR near Groveland, that NCFR also stalled, suggesting that this may be an important component of a high-impact NCFR event. These events demonstrate the presence and importance of NCFRs in the northern and central California regions. However, a more in-depth exploration into their frequency and characteristics is needed to better understand their impacts on both short-term hazard as well as the long-term geomorphic evolution of the region.

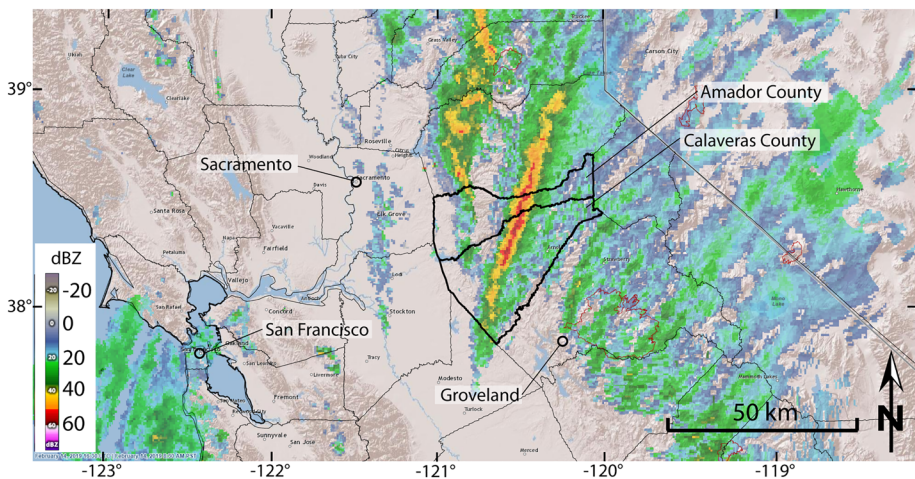


Figure 9. Radar reflectivity (dBZ) during a probable NCFR on 14 February 2019 at 16:30 UTC (8:30 a.m. PST) that caused flooding and landslides in the Sierra Nevada foothills of northern California. Levels of dBZ > 50 (red color) indicate very intense rainfall. Radar data are from NOAA (<https://www.cnrfc.noaa.gov/radarArchive.php>; accessed on 18 March 2020).

Looking more broadly at NCFRs and impacts worldwide, we find only a few examples where the landscape response has been well documented, but these support our view that considering mesoscale effects is critically important to understanding landscape response and resultant hazards from storm rainfall. For example, recent work in southern California found that approximately one third of investigated postfire debris flows for which coincident storm radar imagery was available were related to NCFRs (Oakley et al., 2017), including the fatal 2018 postfire debris flows in Montecito, California (Oakley, Cannon, et al., 2018). Further, Cannon et al. (2018) noted an NCFR in 2017 that produced intense precipitation in the vicinity of the Santa Ana River watershed in southern California and suggested that NCFRs associated with atmospheric rivers be further investigated to compare orographic rain rates and NCFR-driven rain rates in the region so that the hazards that they produce might be better evaluated. Although NCFRs have been observed and described from a meteorological standpoint in other midlatitude regions of the world (e.g., Gatzen, 2011; James & Browning, 1979; Roux et al., 1993; Viale et al., 2013), connections have not been drawn between these events and landscape impacts. Based on our observations from the 22 March 2018 event and other events described herein, we propose that a relationship is likely; evaluating this relationship could be a key avenue for future synchronized interdisciplinary research.

6.4. Mesoscale Features and Geomorphic Hazards

We have focused our discussion about mesoscale meteorological relationships with landscape response on NCFR events specifically, but the literature contains examples of analogous relationships with other types of mesoscale meteorological conditions as well. These may also serve as starting points for future geometeorological studies. Whereas intense storm rainfall can cause extreme, landscape-resetting geomorphic change and sediment mobilization in a wide variety of settings worldwide (e.g., Casalbore et al., 2011; Hobley et al., 2012; Le Lay & Saulnier, 2007; Rodríguez-Blanco et al., 2020), geomorphological investigations of such occurrences rarely include detailed examination of the meteorological forcing causing such events. The mesoscale mechanisms resulting in extreme landscape change therefore remain understudied. However, even without a detailed analysis of the meteorological drivers, the geomorphic response patterns may implicate mesoscale processes as a defining driver of landscape change. A prominent example is a severe storm that affected mountainous terrain in Ladakh, northern India, in August 2010. There, Hobley et al. (2012) reported major flooding, landslides, and debris flows that killed 600 people and devastated 60 villages. Based on the landslide and debris flow distribution, Hobley et al. (2012) concluded that the responsible storm rainband had been only 6 km wide, but had produced 75 mm of rain in 30 min, 1.5 times the 100-year precipitation event for that region. Thus, mesoscale meteorological conditions were more than likely responsible for generating the observed landscape-resetting geomorphic response.

Hurricanes (also called typhoons or tropical cyclones depending on their location) may serve as another topical example that could benefit from additional focused studies. Notably, hurricanes are a well-studied meteorological phenomenon (e.g., Burpee, 1986) with a direct causal relationship to landsliding (e.g., Bessette-Kirton et al., 2019; Negri et al., 2005). However, most hurricane-induced landslide investigations have focused on developing threshold relationships based solely on ground-based rainfall measurements without a full understanding of the mesoscale features embedded within them that might deliver copious rainfall in one place but not another. The reasons for this are well noted—namely, landslide scientists and hazard planners are generally more focused on predicting the effects, regardless of the exact causal phenomena. However, meteorological studies exist that have attempted to tease out additional understanding. Analysis of the precipitation patterns during Hurricane Dean in 2007 over the island of Dominica in the West Indies (Smith et al., 2009) found that stationary cyclonic spiral bands were at least partially responsible for increased rainfall totals and resultant fatal landslides. Similarly, several debris flows in the southeastern United States from Hurricane Ivan in 2004 were also linked to the passage of spiral rain bands over the region (Wooten et al., 2008). Although these studies did not investigate direct causal relationship with the spatial distribution of all landslides from the events, the data and mesoscale understanding (along with orographic effects) may provide impetus for future similar investigations. These could then aid predictive models for expected landslide distributions from hurricanes having similar mesoscale features.

Mesoscale features could also be used to identify the precise meteorological conditions under which debris flows occur in continental climates (such as those studied by Hobley et al., 2012, in northern India, discussed previously). Debris flows that resulted from the September 2013 Colorado Front Range storm event, the number of which was historically unprecedented in that region, provide an excellent example for this pursuit (Anderson et al., 2015; Coe et al., 2014; Patton et al., 2018). Though orographic lift was a key process in precipitation generation in that storm, mesoscale circulation features influenced the spatial pattern of rainfall such that storm total precipitation maxima were not aligned with the orographic slope (Gochis et al., 2015). Rather, intense precipitation (with 10-min rainfall intensities in excess of 60 mm/hr⁻¹; Coe et al., 2014) resulted from the merging of two areas of low-level enhanced convergence and intense convection over the region most heavily impacted by debris flows (1,138 total over a 3,420 km² region; Coe et al., 2014). By comparing debris flow timing to low-level wind observations and radar reflectivity data from the 2013 Front Range event (Gochis et al., 2015), it is evident that debris flow occurrence was coincident with mesoscale convective features of the storm. An analogous example of debris flows generated by mesoscale convection, albeit with a different triggering mechanism (multiday cumulative storm totals rather than intense precipitation) occurred in southeastern Arizona (Griffiths et al., 2009) where mesoscale convective systems reformed each night for five days in the same region and led to cumulative precipitation totals exceeding 50-year recurrence intervals. These examples all indicate a need to consider mesoscale meteorological conditions, rather than macro (synoptic) scale or spatially and temporally averaged storm conditions, to be the likely driver of extreme landscape response and especially of how and where serious storm-induced hazards develop on a landscape.

The use of both radar data and mesoscale model output can provide valuable information for geomorphologists and emergency responders, especially in ungauged and remote locations. For example, this information can inform the decision whether to deploy staff to a study site following a rainfall event if precipitation exceeded thresholds of interest. In addition, forecasts of mesoscale features known to produce high-intensity rainfall that are affecting an area of concern may assist in the positioning of emergency response resources. Although current meteorological forecasting methods are limited in their capability to provide the exact location, timing, and precipitation intensity associated with mesoscale features (e.g., Schwartz, 2014), mesoscale models can serve as a useful tool for situational awareness and regional guidance for localized high-intensity rainfall that may cause a landscape response (e.g., Cannon et al., 2020). Operational radar data and radar-derived precipitation products are also informative, but their utility is limited in this study area and for areas of complex terrain in general. For the 22 March 2018 storm, radar reflectivity was critical for identifying the NCFR (Figure 2). However, due to factors such as radar beam blockage, beam height and coverage in the area, and the lack of suitable reflectivity-rainfall (Z-R) relationship for the particular meteorological situation at hand, quantitative estimates of cumulative rainfall and rainfall intensity were not in agreement with recorded rain gauge data (see Text SB, Figures SB8 and SB9). These limitations can be overcome in areas of complex terrain through the installation of gap-filling radar networks (e.g., Johnson

et al., 2020) or the deployment of mobile radars to areas of particular concern (e.g., Jorgensen et al., 2011). Though some progress has been made to improve Z-R relationships for cool season storms in the western United States (e.g., Cifelli et al., 2018; Matrosov et al., 2014), efforts to further constrain these relationships, especially for shallow convective features such as NCFRs, are needed.

7. Conclusions

Meteorological forcing can cause extreme landscape change through delivery of intense and/or long-duration rainfall. However, linkages between the particular meteorological features that lead to rainfall enhancement and the resultant landscape change have generally received little attention from the geomorphologic and landslide hazard communities. Although synoptic-scale features such as hurricanes and atmospheric rivers (AR) are well-known to deliver copious precipitation causing widespread flooding and damage, mesoscale features such as squall lines and rainbands are also capable of intense precipitation with similar, but more localized, effects. In this study, we presented a detailed examination of one type of mesoscale feature: the narrow cold frontal rainband (NCFR). The NCFR event that we selected for analysis led to regional flash flooding with infrastructure damage in the tens of millions of dollars, caused hundreds of landslides, and resulted in a localized, 1-day sediment flux to a major river system that was up to 16 times the average annual sediment yield for the watershed. The enhanced damage may have been due to the intense precipitation associated with the NCFR occurring after a strong AR had nearly saturated the landscape in the hours prior to NCFR arrival. We noted several examples of impactful NCFRs in our greater study region (northern California) that suggest a direct connection between mesoscale-related intense precipitation and localized extreme landscape effects and related damage to communities and infrastructure. We therefore argue that NCFRs are features worthy of recognition and additional investigation. As such, they may be important features to consider in the assessment and early warning for geomorphic hazards such as landslides.

Acknowledgments

Thanks are due to Joshua Logan (USGS) and Ian Buckley for their assistance with field work, and Stephen Low (USGS) for performing grain size analyses on field samples. We also thank Curtis Kvamme and Bob Stanley (U.S. Forest Service) for access and field assistance within the Stanislaus National Forest and along the Tuolumne River; Joe Wagenbrenner (U.S. Forest Service) for rain-gauge data from research sites within the Stanislaus National Forest; Chad Hecht and Brian Kawzenuk at the Center for Western Weather and Water Extremes (CW3E) at Scripps Institution of Oceanography (SIO) for support in creating meteorological reanalysis plots; Forest Cannon (SIO/CW3E) for productive discussions; Warren Blier, Brian Brong, and Michelle Mead of the National Weather Service for assistance with meteorological data retrieval and interpretation, and information on warning products issued during the 22 March 2018 storm; and OARS of California for river rafting support during our field work. Finally, we thank Benjamin Mirus (USGS), Dalia Kirschbaum (NASA), Jonathan Gourley (NOAA), an anonymous reviewer, and Associate Editor Adam Booth for constructive reviews of earlier versions of the manuscript that improved the content and delivery of this research. Any trade names mentioned in the paper are for descriptive purposes only and do not constitute endorsement by the U.S. government.

Although we focused on the presence and impacts of NCFRs in this study, other mesoscale features (e.g., spiral rainbands in hurricanes, mesoscale convection in continental mountain environments) are also worthy of attention to explain extreme landscape effects that result from storms. To best predict and be prepared for hazards associated with these effects, studies should therefore incorporate the mesoscale atmospheric processes that are capable of producing localized intense precipitation. Whereas many landscape processes (e.g., landslides, sediment transport) depend on exceeding a threshold forcing, landscape effects often respond in a nonlinear fashion to linear increases in the driving force (e.g., rainfall intensity causing saturation or runoff causing shear stress) beyond the process threshold. Understanding and predicting the spatial distribution of high-intensity precipitation events associated with various mesoscale meteorological phenomena should help identify when and where these thresholds may be exceeded. Further integration between the geomorphology, hydrology, and meteorology communities will advance important scientific goals for all, and ultimately improve predictions related to storm characteristics and geohazards.

Data Availability Statement

Data from this study, including all supporting information files and figures, can be accessed online via the USGS's ScienceBase data repository (<https://doi.org/10.5066/P9BU8FAQ>).

References

- Abney, R. B., Kuhn, T. J., Chow, A., Hockaday, W., Fogel, M. L., & Berhe, A. A. (2019). Pyrogenic carbon erosion after the Rim Fire, Yosemite National Park: The role of burn severity and slope. *Journal of Geophysical Research: Biogeosciences*, 124, 432–449. <https://doi.org/10.1029/2018JG004787>
- Anderson, S. W., Anderson, S. P., & Anderson, R. S. (2015). Exhumation by debris flows in the 2013 Colorado Front Range storm. *Geology*, 43, 391–394. <https://doi.org/10.1130/G36507.1>
- Bellmore, J. R., & Baxter, C. V. (2014). Effects of geomorphic process domains on river ecosystems: A comparison of floodplain and confined valley segments. *River Research and Applications*, 30(5), 617–630. <https://doi.org/10.1002/rra.2672>
- Bessette-Kirton, E. K., Cerovski-Darriau, C., Schulz, W. H., Coe, J. A., Kean, J. W., Godt, J. W., et al. (2019). Landslides triggered by Hurricane Maria: An assessment of an extreme event in Puerto Rico. *GSA Today*, 29(6), 4–10. <https://doi.org/10.1130/GSATG383A.1>
- Blier, W. (2003). An examination of an intense landfalling narrow cold frontal rainband using the Weather Event Simulator (WES), National Weather Service–Technical Attachment Lite 03–13, 9p. https://www.weather.gov/media/wrh/online_publications/talite/talite0313.pdf, accessed 25 April 2020.
- Blier, W., Monteverdi, J. P., & Null, J. (2005). *The historic San Francisco flash flood event of 25 February 2004*. Paper presented at Proceedings of the 6th Conference on Coastal Atmospheric and Oceanic Prediction and Processes (pp. 1–5). Retrieved from https://ams.confex.com/ams/Annual2005/techprogram/paper_84208.htm, accessed 25 April 2020.

- Browning, K. A. (1986). Conceptual models of precipitation systems. *Weather and Forecasting*, 1, 23–41. [https://doi.org/10.1175/1520-0434\(1986\)001%3C0023:CMOPS%3E2.0.CO;2](https://doi.org/10.1175/1520-0434(1986)001%3C0023:CMOPS%3E2.0.CO;2)
- Browning, K. A., & Harrold, T. W. (1970). Air motion and precipitation growth at a cold front. *Quarterly Journal of the Royal Meteorological Society*, 96, 369–389. <https://doi.org/10.1002/qj.49709640903>
- Burpee, R. W. (1986). Mesoscale structure of hurricanes. In P. S. Ray (Ed.), *Mesoscale meteorology and forecasting* (pp. 311–330). Boston, MA: American Meteorological Society.
- Caine, N. (1980). The rainfall intensity-duration control of shallow landslides and debris flows. *Geografiska Annaler Series A, Physical Geography*, 62(1–2), 23–27. <https://doi.org/10.1080/04353676.1980.1187996>
- Cannon, F., Hecht, C. W., Cordeira, J. M., & Ralph, F. M. (2018). Synoptic and mesoscale forcing of Southern California extreme precipitation. *Journal of Geophysical Research: Atmospheres*, 123, 13,714–13,730. <https://doi.org/10.1029/2018JD029045>
- Cannon, F., Oakley, N. S., Hecht, C. W., Michaelis, A., Cordeira, J. M., Kawzenuk, B., et al. (2020). Observations and predictability of a high-impact narrow cold-frontal rainband over southern California on 2 February 2019. *Weather and Forecasting*, Advance online publication, 35(5), 2083–2097. <https://doi.org/10.1175/WAF-D-20-0012.1>
- Cannon, S. H. (1988). Regional rainfall-threshold conditions for abundant debris-flow activity. In S. D. Ellen, & G. F. Wieczorek (Eds.), *Landslides, floods, and marine effects of the storm of January 3–5, 1982, in the San Francisco Bay Region, California, U.S. Geological Survey Professional Paper 1434* (pp. 35–42). Washington, DC: U.S. Geological Survey. <https://doi.org/10.3133/pp1434>
- Casalbore, D., Chiocci, F. L., Mugnozza, G. S., Tommasi, P., & Sposato, A. (2011). Flash-flood hyperpycnal flows generating shallow-water landslides at Fiumara mouths in Western Messina Strait (Italy). *Marine Geophysical Research*, 32, 257–271. <https://doi.org/10.1007/s11001-011-9,128-y>
- Casas, A., Garcia, M., Siegel, R. B., Koltunov, A., Ramirez, C., & Ustin, S. (2016). Burned forest characterization at single-tree level with airborne laser scanning for assessing wildlife habitat. *Remote Sensing of Environment*, 175, 231–241. <https://doi.org/10.1016/j.rse.2015.12.044>
- Cifelli, R., Chandrasekar, V., Chen, H., & Johnson, L. E. (2018). High resolution radar quantitative precipitation estimation in the San Francisco Bay Area: Rainfall monitoring for the urban environment. *Journal of the Meteorological Society of Japan Series II*, 96A, 141–155. <https://doi.org/10.2151/jmsj.2018-016>
- Coe, J. A., Kean, J. W., Godt, J. W., Baum, R. L., Jones, E. S., Gochis, D. J., & Anderson, G. S. (2014). New insights into debris-flow hazards from an extraordinary event in the Colorado Front Range. *GSA Today*, 24(10), 4–10. <https://doi.org/10.1130/GSATG214A.1>
- Collins, B. D., & Znidarcic, D. (2004). Stability analyses of rainfall induced landslides. *Journal of Geotechnical and Geoenvironmental Engineering*, 130(4), 362–372. [https://doi.org/10.1061/\(ASCE\)1,090-0241\(2004\)130:4\(362\)](https://doi.org/10.1061/(ASCE)1,090-0241(2004)130:4(362))
- Cordeira, J., Stock, J., Dettinger, M., Young, A., Kalansky, J., & Ralph, F. M. (2019). A 142-yr climatology of northern California landslides and atmospheric rivers. *Bulletin of the American Meteorological Society*, 100, 1499–1509. <https://doi.org/10.1175/BAMS-D-18-0158.1>
- Gatzen, C. (2011). A 10-year climatology of cold-season narrow cold-frontal rainbands in Germany. *Atmospheric Research*, 100(4), 366–370. <https://doi.org/10.1016/j.atmosres.2010.09.018>
- Gelaro, R., McCarty, W., Suarez, M. J., Todling, R., Molod, A., Takacs, L., et al. (2017). The modern-era retrospective analysis for research and applications, Version 2 (MERRA-2). *Journal of Climate*, 30(14), 5419–5454. <https://doi.org/10.1175/JCLI-D-16-0758.1>
- Gochis, D., Schumacher, R., Friedrich, K., Doesken, N., Kelsch, M., Sun, J., et al. (2015). The great Colorado flood of September 2013. *Bulletin of the American Meteorological Society*, 96(9), 1461–1487. <https://doi.org/10.1175/BAMS-D-13-00241.1>
- Godt, J. W., & Coe, J. A. (2007). Alpine debris flows triggered by a 28 July 1999 thunderstorm in the central Front Range, Colorado. *Geomorphology*, 84(1–2), 80–97. <https://doi.org/10.1016/j.geomorph.2006.07.009>
- Greig, S. M., Sear, D. A., & Carling, P. A. (2005). The impact of fine sediment accumulation on the survival of incubating salmon progeny: Implications for sediment management. *Science of the Total Environment*, 344, 241–258. <https://doi.org/10.1016/j.scitotenv.2005.02.010>
- Griffiths, P. G., Magirl, C. S., Webb, R. H., Pytlak, E., Troch, P. A., & Lyon, S. W. (2009). Spatial distribution and frequency of precipitation during an extreme event: July 2006 mesoscale convective complexes and floods in southeastern Arizona. *Water Resources Research*, 45, W07419. <https://doi.org/10.1029/2008WR007380>
- Guzzetti, F., Peruccacci, S., Rossi, M., & Stark, C. (2008). The rainfall intensity-duration control of shallow landslides and debris flows - an update. *Landslides*, 5(3), 3–17. <https://doi.org/10.1007/s10346-007-0112-1>
- Guzzetti, F., Reichenbach, P., Cardinali, M., Galli, M., & Ardizzone, F. (2005). Probabilistic landslide hazard assessment at the basin scale. *Geomorphology*, 72, 272–299. <https://doi.org/10.1016/j.geomorph.2005.06.002>
- Hatchett, B. J. (2018). Snow level characteristics and impacts of a spring typhoon-originating atmospheric river in the Sierra Nevada, USA. *Atmosphere*, 9, 233. <https://doi.org/10.3390/atmos9060233>
- Hatchett, B. J., Cao, Q., Dawson, P. B., Ellis, C. J., Hecht, C. W., Kawzenuk, B., et al. (2020). Observations of an extreme atmospheric river storm with a diverse sensor network. *Earth and Space Science*, 7, e2020EA001129. <https://doi.org/10.1029/2020EA001129>
- Hauer, C., Unfer, G., Tritthart, M., & Habersack, H. (2011). Effects of stream channel morphology, transport processes and effective discharge on salmonid spawning habitats. *Earth Surface Processes and Landforms*, 36, 672–685. <https://doi.org/10.1002/esp.2087>
- HDR Engineering, Inc (2012). Don Pedro Reservoir bathymetric study report, Prepared for Turlock Irrigation District and Modesto Irrigation District, Turlock and Modesto, California (p. 8). http://www.donpedro-relicensing.com/Lists/Announcements/Attachments/84/DonPedroReservoirBathymetricStudyRept_20121018.pdf, accessed 25 April 2020
- Hobbs, P. V. (1978). Organization and structure of clouds and precipitation on the mesoscale and microscale in cyclonic storms. *Reviews of Geophysics*, 16(4), 741–755. <https://doi.org/10.1029/RG016i004p00741>
- Hobbs, P. V., & Biswas, K. R. (1979). The cellular structure of narrow cold-frontal rainbands. *Quarterly Journal of the Royal Meteorological Society*, 105, 723–727. <https://doi.org/10.1002/qj.49710544516>
- Hobbs, P. V., & Persson, P. O. (1982). The mesoscale and microscale structure and organization of clouds and precipitation in midlatitude cyclones. Part V: The substructure of narrow cold-frontal rainbands. *Journal of the Atmospheric Sciences*, 39, 280–295. [https://doi.org/10.1175/1520-0469\(1982\)039<0280:TMAMSA>2.0.CO;2](https://doi.org/10.1175/1520-0469(1982)039<0280:TMAMSA>2.0.CO;2)
- Hobley, D. E. J., Sinclair, H. D., & Mudd, S. M. (2012). Reconstruction of a major storm event from its geomorphic signature. *Geology*, 40(6), 483–486. <https://doi.org/10.1130/G32935.1>
- Hooke, J. M. (2015). Variations in flood magnitude-effect relations and the implications for flood risk assessment and river management. *Geomorphology*, 251, 91–107. <https://doi.org/10.1016/j.geomorph.2015.05.014>
- Houze, R. A., Hobbs, P. V., Biswas, K. R., & Davis, W. M. (1976). Mesoscale rainbands in extratropical cyclones. *Monthly Weather Review*, 104, 868–878. [https://doi.org/10.1175/1520-0493\(1976\)104%3C0868:MRIEC%3E2.0.CO;2](https://doi.org/10.1175/1520-0493(1976)104%3C0868:MRIEC%3E2.0.CO;2)
- James, P. K., & Browning, K. A. (1979). Mesoscale structure of line convection at surface cold fronts. *Quarterly Journal of the Royal Meteorological Society*, 105(444), 371–382. <https://doi.org/10.1002/qj.49710544404>

- Johnson, L. E., Cifelli, R., & White, A. (2020). Benefits of an advanced quantitative precipitation information system. *Journal of Flood Risk Management*, 13, e12573. <https://doi.org/10.1111/jfr3.12573>
- Jorgensen, D. P., Hanshaw, M. N., Schmidt, K. M., Laber, J. L., Staley, D. M., Kean, J. W., & Restrepo, P. J. (2011). Value of a dual-polarized gap-filling radar in support of southern California post-fire debris-flow warnings. *Journal of Hydrometeorology*, 12, 1581–1595. <https://doi.org/10.1175/JHM-D-11-05.1>
- Jorgensen, D. P., Pu, Z., Persson, P. O., & Tao, W. (2003). Variations associated with cores and gaps of a Pacific narrow cold frontal rainband. *Monthly Weather Review*, 131, 2705–2729. [https://doi.org/10.1175/1520-0493\(2003\)131<2705:VAWCAG>2.0.CO;2](https://doi.org/10.1175/1520-0493(2003)131<2705:VAWCAG>2.0.CO;2)
- Kean, J. W., Staley, D. M., Lancaster, J. T., Rengers, F. K., Swanson, B. J., Coe, J. A., et al. (2019). Inundation, flow dynamics, and damage in the 9 January 2018 Montecito debris-flow event, California, USA. Opportunities and challenges for post-wildfire risk assessment. *Geosphere*, 15(4), 1140–1163. <https://doi.org/10.1130/GES02048.1>
- King, K. C., Kaplan, M., & Smallcomb, C. C. (2009). *Development and propagation of a narrow cold frontal rain band in the Sierra Nevada of northern California*. Paper presented at Proceedings of the 13th Conference on Mesoscale Processes, American Meteorological Society.
- Koch, S. E., & Kocin, P. J. (1991). Frontal contraction processes leading to the formation of an intense narrow rainband. *Meteorology and Atmospheric Physics*, 46(3–4), 123–154. <https://doi.org/10.1007/BF01027339>
- Lappala, E. G., Healy, R. W., & Weeks, E. P. (1987). *Documentation of computer program VS2D to solve the equations of fluid flow in variably saturated porous media*. U.S. Geological Survey Water Resources Investigations Report 83-4099. U.S. Geological Survey Water Resources Investigations Report 83-4099 (pp. 1–184). <https://doi.org/10.3133/wri834099>
- Le Lay, M., & Saulnier, G. M. (2007). Exploring the signature of climate and landscape spatial variabilities in flash flood events: Case of the 8–9 September 2002 Cévennes-Vivarais catastrophic event. *Geophysical Research Letters*, 34, L13401. <https://doi.org/10.1029/2007GL029746>
- Lin, Y. L. (2007). *Mesoscale dynamics* (pp. 1–646). Cambridge: Cambridge University Press. <https://doi.org/10.1017/CBO9780511619649>
- Lisenby, P. E., Croke, J., & Fryirs, K. A. (2018). Geomorphic effectiveness: a linear concept in a non-linear world. *Earth Surface Processes and Landforms*, 43, 4–20. <https://doi.org/10.1002/esp.4096>
- Locatelli, J. D., Martin, J. E., & Hobbs, P. V. (1995). Development and propagation of precipitation cores on cold fronts. *Atmospheric Research*, 38(1–4), 177–206. [https://doi.org/10.1016/0169-8095\(94\)00093-S](https://doi.org/10.1016/0169-8095(94)00093-S)
- Marécal, V., Hauser, D., & Roux, F. (1993). The 12/13 January 1988 narrow cold-frontal rainband observed during MFDP/FRONTS 87. Part II: Microphysics. *Journal of the Atmospheric Sciences*, 50, 975–998. [https://doi.org/10.1175/1520-0469\(1993\)050<975:T12/13>2.0.CO;2](https://doi.org/10.1175/1520-0469(1993)050<975:T12/13>2.0.CO;2)
- Markowski, P., & Richardson, Y. (2010). *Mesoscale meteorology in midlatitudes* (pp. 1–407). West Sussex: John Wiley & Sons. <https://doi.org/10.1002/9780470682104>
- Matrosov, S. Y., Ralph, F. M., Neiman, P. J., & White, A. B. (2014). Quantitative assessment of operational weather radar rainfall estimates over California's Northern Sonoma County using HMT-West data. *Journal of Hydrometeorology*, 15, 393–410. <https://doi.org/10.1175/JHM-D-13-045.1>
- McGuire, L. A., Rengers, F. K., Kean, J. W., Coe, J. A., Mirus, B. B., Baum, R. L., & Godt, J. W. (2016). Elucidating the role of vegetation in the initiation of rainfall-induced shallow landslides: Insights from an extreme rainfall event in the Colorado Front Range. *Geophysical Research Letters*, 43, 9084–9092. <https://doi.org/10.1002/2016GL070741>
- Meadows, J., Mattarochia, K., Bollenbacher, A., & Kahler, C. (2019). *Debris flow and flash flood impact decision support services within a postwildfire environment*. Paper presented at Proceedings of the 99th Annual Meeting. Retrieved from <https://ams.confex.com/ams/2019Annual/webprogram/Paper350263.html>, accessed 27 March 2020
- MesoWest. (2019). *5-minute precipitation data from rail road flat* (Station WA5KWK, AT317). Calaveras County, CA: MesoWest Network. Retrieved from <https://mesowest.utah.edu/>, accessed 30 Dec 2019
- Mirus, B. B., & Loague, K. (2013). How runoff begins (and ends): Characterizing hydrologic response at the catchment scale. *Water Resources Research*, 49, 2987–3006. <https://doi.org/10.1002/wrcr.20218>
- Mollie, S., Jouet, G., Freslon, N., Bourles, D. L., Authemayou, C., Moreau, J., & Rabineau, M. (2017). Controls on Holocene denudation rates in mountainous environments under Mediterranean climate. *Earth Surface Processes and Landforms*, 42, 272–289. <https://doi.org/10.1002/esp.3987>
- Moody, J. A., Shakesby, R. A., Robichaud, P. R., Cannon, S. H., & Martin, D. A. (2013). Current research issues related to post-wildfire runoff and erosion processes. *Earth Science Reviews*, 122, 10–37. <https://doi.org/10.1016/j.earscirev.2013.03.004>
- Negri, A. J., Burkardt, N., Golden, J. H., Halverson, J. B., Huffman, G. J., Larsen, M. C., et al. (2005). The hurricane–flood–landslide continuum. *Bulletin of the American Meteorological Society*, 86(9), 1241–1247. <https://doi.org/10.1175/BAMS-86-9-1241>
- Neiman, P. J., Hughes, M., Moore, B. J., Ralph, F. M., & Sukovich, E. M. (2013). Sierra barrier jets, atmospheric rivers, and precipitation characteristics in northern California: a composite perspective based on a network of wind profilers. *Monthly Weather Review*, 141, 4211–4233. <https://doi.org/10.1175/MWR-D-13-00112.1>
- Neiman, P. J., Martin, R. F., Persson, P. O. G., White, A. B., Jorgensen, D. P., & Kingsmill, D. E. (2004). Modification of fronts and precipitation by coastal blocking during an intense landfalling winter storm in southern California: Observations during CALJET. *Monthly Weather Review*, 132(1), 242–273. [https://doi.org/10.1175/1520-0493\(2004\)132<242:MOFAPB>2.0.CO;2](https://doi.org/10.1175/1520-0493(2004)132<242:MOFAPB>2.0.CO;2)
- NOAA (2020). National Oceanic and Atmospheric Administration ESRL PSD profiler network data and image library. <https://www.esrl.noaa.gov/psd/data/obs/datadisplay/>, accessed 6 April 2020
- Norbiato, D., Borga, M., Merz, R., Blöschl, G., & Carton, A. (2008). Flash flood warning based on rainfall depth-duration thresholds and soil moisture conditions: An assessment for gauged and ungauged basins. *Journal of Hydrology*, 362, 274–290. <https://doi.org/10.1016/j.jhydrol.2008.08.023>
- NPS (2013). National Park Service, Yosemite National Park, Rim Fire 2013 burned area emergency response plan. (p. 99). https://www.nps.gov/yose/learn/management/upload/RIM_BAER_PLAN2013.pdf, accessed 15 January 2020
- Oakley, N. S., Cannon, F., Munroe, R., Lancaster, J. T., Gomberg, D., & Ralph, F. M. (2018). Brief communication: Meteorological and climatological conditions associated with the 9 January 2018 post-fire debris flows in Montecito and Carpinteria California, USA. *Natural Hazards and Earth System Sciences*, 18, 3037–3043. <https://doi.org/10.5194/nhess-18-3037-2018>
- Oakley, N. S., Lancaster, J. T., Hatchett, B. J., Stock, J., Ralph, F. M., Roj, S., & Lukashov, S. (2018). A 22-year climatology of cool season hourly precipitation thresholds conducive to shallow landslides in California. *Earth Interactions*, 22, 1–35. <https://doi.org/10.1175/EI-D-17-0029.1>
- Oakley, N. S., Lancaster, J. T., Kaplan, M. L., & Ralph, F. M. (2017). Synoptic conditions associated with cool season post-fire debris flows in the Transverse Ranges of Southern California. *Natural Hazards*, 88(1), 327–354. <https://doi.org/10.1007/s11069-017-2867-6>

- Parise, M., & Cannon, S. H. (2012). Wildfire impacts on the processes that generate debris flows in burned watersheds. *Natural Hazards*, 61(1), 217–227. <https://doi.org/10.1007/s11069-011-9769-9>
- Patton, A. I., Rathburn, S. L., Bilderback, E. L., & Lukens, C. E. (2018). Patterns of debris flow initiation and periglacial sediment sourcing in the Colorado Front Range. *Earth Surface Processes and Landforms*, 43, 2998–3008. <https://doi.org/10.1002/esp.4463>
- Persson, P. O. G., Neiman, P. J., Walter, B., Bao, J. W., & Ralph, F. M. (2005). Contributions from California coastal-zone surface fluxes to heavy coastal precipitation: A CALJET case study during the strong El Niño of 1998. *Monthly Weather Review*, 133(5), 1175–1198. <https://doi.org/10.1175/MWR2910.1>
- Phillips, J. D. (2006). Evolutionary geomorphology: thresholds and nonlinearity in landform response to environmental change. *Hydrology and Earth System Sciences*, 10, 731–742. <https://doi.org/10.5194/hess-10-731-2006>
- Postance, B., Hillier, J., Dijkstra, T., & Dixon, N. (2018). Comparing threshold definition techniques for rainfall-induced landslides: a national assessment using radar rainfall. *Earth Surface Processes and Landforms*, 43, 553–560. <https://doi.org/10.1002/esp.4202>
- Ralph, F. M., Coleman, T., Neiman, P. J., Zamora, R. J., & Dettinger, M. D. (2013). Observed impacts of duration and seasonality of atmospheric-river landfalls on soil moisture and runoff in coastal Northern California. *Journal of Hydrometeorology*, 14, 443–459. <https://doi.org/10.1175/JHM-D-12-076.1>
- Ralph, F. M., & Neiman, P. J. (2005). Dropsonde observations in low-level jets over the northeastern Pacific Ocean from CALJET-1998 and PACJET-2001: mean vertical-profile and atmospheric-river characteristics. *Monthly Weather Review*, 133, 889–910. <https://doi.org/10.1175/MWR2896.1>
- Ralph, F. M., Neiman, P. J., Wick, G. A., Gutman, S. I., Dettinger, M. D., Cayan, D. R., & White, A. B. (2006). Flooding on California's Russian River: role of atmospheric rivers. *Geophysical Research Letters*, 33, L13801. <https://doi.org/10.1029/2006GL026689>
- Ralph, F. M., Rutz, J. J., Cordeira, J. M., Dettinger, M., Anderson, M., Reynolds, D., et al. (2019). A scale to characterize the strength and impacts of atmospheric rivers. *Bulletin of the American Meteorological Society*, 100(2), 269–289. <https://doi.org/10.1175/BAMS-D-18-0023.1>
- Rodríguez-Blanco, M. L., Taboada-Castro, M. M., & Taboada-Castro, M. T. (2020). Suspended sediment dynamics during a period of consecutive explosive cyclogenesis in rural temperate catchments: a case study from small-sized catchments in NW Spain. *Catena*, 187, 104316. <https://doi.org/10.1016/j.catena.2019.104316>
- Roux, F., Marécal, V., & Hauser, D. (1993). The 12/13 January 1988 narrow cold-frontal rainband observed during MFDP/FRONTS 87. Part I: kinematics and thermodynamics. *Journal of Atmospheric Sciences*, 50(7), 951–974. [https://doi.org/10.1175/1520-0469\(1993\)050<0951:TJNCFR>2.0.CO;2](https://doi.org/10.1175/1520-0469(1993)050<0951:TJNCFR>2.0.CO;2)
- Rutledge, S. A., & Hobbs, P. V. (1984). The mesoscale and microscale structure and organization of clouds and precipitation in midlatitude cyclones. XII: A diagnostic modeling study of precipitation development in narrow cold-frontal rainbands. *Journal of the Atmospheric Sciences*, 41, 2949–2972. [https://doi.org/10.1175/1520-0469\(1984\)04<2949:TMAMSA>2.0.CO;2](https://doi.org/10.1175/1520-0469(1984)04<2949:TMAMSA>2.0.CO;2)
- Schmidt, K. M., Roering, J. J., Stock, J. D., Dietrich, W. E., Montgomery, D. R., & Schaub, T. (2001). The variability of root cohesion as an influence on shallow landslide susceptibility in the Oregon Coast Range. *Canadian Geotechnical Journal*, 38, 995–1024. <https://doi.org/10.1139/t01-031>
- Schumacher, P. N., Knight, D. J., & Bosart, L. F. (1996). Frontal interaction with the Appalachian Mountains, Part I: A climatology. *Monthly Weather Review*, 124(11), 2453–2468. [https://doi.org/10.1175/1520-0493\(1996\)124<2453:FIWTAM>2.0.CO;2](https://doi.org/10.1175/1520-0493(1996)124<2453:FIWTAM>2.0.CO;2)
- Schumm, S. A. (1979). Geomorphic thresholds: the concept and its applications. *Transactions of the Institute of British Geographers*, 4(4), 485–515. <https://www.jstor.org/stable/622211>
- Schwanghart, W., & Scherler, D. (2014). Short Communication: TopoToolbox 2 – an efficient and user-friendly tool for Earth surface sciences. *Earth Surface Dynamics Discussions*, 2(1), 1–7. <https://doi.org/10.5194/esurf-2-1-2014>
- Schwartz, C. S. (2014). Reproducing the September 2013 record-breaking rainfall over the Colorado Front Range with high-resolution WRF forecasts. *Weather and Forecasting*, 29(2), 393–402. <https://doi.org/10.1175/WAF-D-13-00136.1>
- Shive, K. L., Estes, B. L., White, A. M., Safford, H. D., O'Hara, K. L., & Stephens, S. L. (2017). Rice straw mulch for post-fire erosion control: assessing non-target effects on vegetation communities. *International Journal of Wildland Fire*, 26(6), 538–549. <https://doi.org/10.1071/WF16208>
- Smith, R. B., Schafer, P., Kirshbaum, D., & Regina, E. (2009). Orographic enhancement of precipitation inside Hurricane Dean. *Journal of Hydrometeorology*, 10(3), 820–831. <https://doi.org/10.1175/2008JHM1057.1>
- Spina, A. P. (2000). Habitat partitioning in a patchy environment: considering the role of intraspecific competition. *Environmental Biology of Fishes*, 57, 393–400. <https://doi.org/10.1023/A:1007682010268>
- Staley, D. M. (2013). *Emergency assessment of post-fire debris-flow hazards for the 2013 Rim Fire, Stanislaus National Forest and Yosemite National Park, California. U.S. Geological Survey Open-File Report 2013-1260* (3 plates, pp. 1–11). Retrieved from <http://pubs.usgs.gov/of/2013/1260/>
- Thunis, P., & Bornstein, R. (1996). Hierarchy of mesoscale flow assumptions and equations. *Journal of Atmospheric Sciences*, 53, 380–397. [https://doi.org/10.1175/1520-0469\(1996\)053<0380:HOMFAA>2.0.CO;2](https://doi.org/10.1175/1520-0469(1996)053<0380:HOMFAA>2.0.CO;2)
- U.S. Geological Survey (1897). Geologic atlas of the United States—Sonora, California Folio, U.S. Geological Survey Geologic Folio 41, <https://pubs.usgs.gov/gf/041/>
- U.S. Geological Survey (2019). National Water Information System records for gaging station 11285500, Tuolumne River at Wards Ferry Bridge near Groveland, California, accessed 13 August 2019. https://nwis.waterdata.usgs.gov/nwis/inventory/%2site_no=11285500%20agency_cd=USGS
- Union Democrat (2018). “March 22 megastorm caused \$74 million in damage”, Sonora Union Democrat Newspaper, accessed 23 April 2018.
- University of Wisconsin (2020). University of Wisconsin Madison Space Science and Engineering Center, MIMIC TPW Ver. 2. <http://tropic.ssec.wisc.edu/real-time/mtpw2/>, accessed 7 April 2020
- van Genuchten, M. T. (1980). A closed-form equation for predicting the hydraulic conductivity of unsaturated soils. *Soil Science Society of America Journal*, 44, 892–898. <https://doi.org/10.2136/sssaj1980.03615995004400050002x>
- Varnes, D. J. (1978). Slope movement types and processes. In R. L. Schuster, & R. J. Krizek (Eds.), *Landslides, analysis and control, Special Report* (Vol. 176, pp. 11–33). Washington, DC: Transportation Research Board, National Academy of Sciences.
- Viale, M., Houze, R. A., & Rasmussen, K. L. (2013). Upstream Orographic enhancement of a narrow cold-frontal rainband approaching the Andes. *Monthly Weather Review*, 141, 1708–1730. <https://doi.org/10.1175/MWR-D-12-00138.1>
- Wagner, D. L., Jennings, C. W., Bedrossian, T. L., & Bortugno, E. J. (1991). Geologic map of the Sacramento quadrangle, California. California Division of Mines and Geology, Regional Geologic Map 1A, 1:250,000.

- White, A. B., Neiman, P. J., Ralph, F. M., Kingsmill, D. E., & Persson, P. O. (2003). Coastal orographic rainfall processes observed by radar during the California land-falling jets experiment. *Journal of Hydrometeorology*, 4, 264–282. [https://doi.org/10.1175/1525-7541\(2003\)4%3C264:CORPOB%3E2.0.CO;2](https://doi.org/10.1175/1525-7541(2003)4%3C264:CORPOB%3E2.0.CO;2)
- Wimmers, A. J., & Velden, C. S. (2011). Seamless advective blending of total precipitable water retrievals from polar-orbiting satellites. *Journal of Applied Meteorology and Climatology*, 50(5), 1024–1036. <https://doi.org/10.1175/2010JAMC2589.1>
- Wohl, E. (2013). The complexity of the real world in the context of the field tradition in geomorphology. *Geomorphology*, 200, 50–58. <https://doi.org/10.1016/j.geomorph.2012.12.016>
- Wooten, R. M., Gillon, K. A., Witt, A. C., Latham, R. S., Douglas, T. J., Bauer, J. B., et al. (2008). Geologic, geomorphic, and meteorological aspects of debris flows triggered by Hurricanes Frances and Ivan during September 2004 in the Southern Appalachian Mountains of Macon County, North Carolina (southeastern USA). *Landslides*, 5(1), 31–44. <https://doi.org/10.1007/s10346-007-0109-9>
- Wright, S. A., & Marineau, M. D. (2019). Turbidity current observations in a large reservoir following a major wildfire. *Journal of Hydraulic Engineering*, 145, 06019011. [https://doi.org/10.1061/\(ASCE\)HY.1943-7900.0001611](https://doi.org/10.1061/(ASCE)HY.1943-7900.0001611)
- Zhu, Y., & Newell, R. E. (1998). A proposed algorithm for moisture fluxes from atmospheric rivers. *Monthly Weather Review*, 126, 725–735. [https://doi.org/10.1175/1520-0493\(1998\)126%3C0725:APAFMF%3E2.0.CO;2](https://doi.org/10.1175/1520-0493(1998)126%3C0725:APAFMF%3E2.0.CO;2)